The optical manifestation of dispersive field-aligned bursts in auroral breakup arcs

H. Dahlgren,[1] J. L. Semeter,[1] R. A. Marshall,[2] and M. Zettergren[3]

[1]   High-resolution optical observations of a substorm expansion show dynamic auroral rays with surges of luminosity traveling up the magnetic field lines. Observed in ground-based imagers, this phenomenon has been termed auroral flames, whereas the rocket signatures of the corresponding energy dispersions are more commonly known as field-aligned bursts. In this paper, observations of auroral flames obtained at 50 frames/s with a scientific-grade Complementary Metal Oxide Semiconductor (CMOS) sensor (30° × 30° field of view, 30 m resolution at 120 km) are used to provide insight into the nature of the precipitating electrons similar to high-resolution particle detectors. Thanks to the large field of view and high spatial resolution of this system, it is possible to obtain a first-order estimate of the temporal evolution in altitude of the volume emission rate from a single sensor. The measured volume emission rates are compared with the sum of modeled eigenprofiles obtained for a finite set of electron beams with varying energy provided by the TRANSCAR auroral flux tube model. The energy dispersion signatures within each auroral ray can be analyzed in detail during a fraction of a second. The evolution of energy and flux of the precipitation shows precipitation spanning over a large range of energies, with the characteristic energy dropping from 2.1 keV to 0.87 keV over 0.2 s. Oscillations at 2.4 Hz in the magnetic zenith correspond to the period of the auroral flames, and the acceleration is believed to be due to Alfvenic wave interaction with electrons above the ionosphere.

1. Introduction

[2]   Auroral breakup marks the start of the substorm expansion phase, when the energy stored in the magnetosphere during the substorm growth phase is unloaded to the ionosphere through Earthward high-speed plasma flows. Ground-based observations of the aurora show a sudden explosive brightening and rapid poleward expansion of a dynamic display of emission structures. High-resolution images of breakup aurora reveal much fine scale structuring, with widths perpendicular to the geomagnetic field of less than 100 m [*Hallinan and Davis*, 1970; *Trondsen and Cogger*, 2001]. These narrow, irregular arcs were named

[1]Department of Electrical and Computer Engineering and Center for Space Physics, Boston University, Boston, Massachusetts, USA.

[2]Department of Aeronautics and Astronautics, Stanford University, Stanford, California, USA.

[3]Physical Sciences Department, Embry-Riddle Aeronautical University, Daytona Beach, Florida, USA.

Corresponding author: H. Dahlgren, Department of Electrical and Computer Engineering and Center for Space Physics, Boston University, 725 Commonwealth Ave., Boston, MA 02215, USA. (hannad@bu.edu)

breakup arcs by *Goertz* [1981]. In an event study of breakup arcs by *Semeter et al.* [2008], it was found that the phenomenon is not turbulent or chaotic; rather, a strong coherence of the fine scale morphology was observed.

[3]   An apparent phenomenon mostly related to post-breakup aurora is surges of luminosity that can be seen to move up along the geomagnetic field. The apparent upward motion of the emissions is believed to be caused by energy dispersion and a time-of-flight effect where the more energetic electrons arrive first. This kind of optical signature is known as flaming aurora [*Omholt*, 1971], which has been categorized as type *p*2 pulsating auroras. *Cresswell* [1969] investigated the altitude of the release point of electrons on the L = 5.5 field line, by comparing the measured emission brightness with modeled luminosity profiles from different energy electrons as provided by *Rees* [1964]. Release points were found to vary from the equatorial plane to 2.5 R_E along the field line from the observation point. The emission height variation due to the differential energy is a signature of electron acceleration through wave-particle interaction.

[4]   To fully resolve the dynamic processes of breakup arcs requires advanced high-speed optical systems with sensitive low-light detectors. In this paper, we present unique imaging observations of an auroral breakup event, at 30 m resolution at auroral altitudes and at an unprecedented 50 Hz temporal resolution. The measurements are in an Earth-fixed
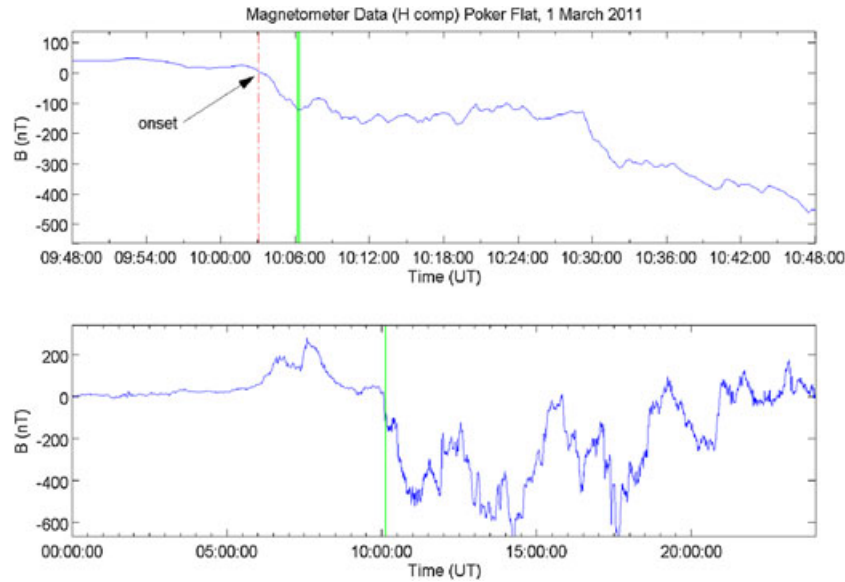
Figure 1. Magnetometer data from the Geophysical Institute Magnetometer Array site at Poker Flat. The top panel shows data from 09:48 UT to 10:48 UT and the bottom panel shows the full day data. The substorm onset takes place at 10:03 UT and is marked with a red dashed line in the top panel. The green block marks the 12 s of optical data available from the high-speed imager.

reference frame allowing for studies of small spatial and temporal variability without ambiguity. Flaming emissions are seen during the event and are analyzed in detail. Comparing the evolution of the volume emission rate with modeled rates obtained from an ionospheric model, the optical data can provide insight into the energy and flux of the precipitating electrons, similar to high-resolution in situ particle detectors.

2. Event and Experiment Description

2.1. Geophysical Conditions

[5] The optical data discussed in this paper were captured from the Poker Flat Rocket Range (65.13°N, 147.47°W) in Alaska during the expansion phase of a substorm on 1 March 2011. At 08:40 UT, the MAG sensor on the ACE satellite measured an interplanetary magnetic field B_z turning from northward to southward, allowing for reconnection and entry of solar wind energy into the magnetosphere. The ACE spacecraft is located at $\sim$199 R_E, resulting in a propagation delay from ACE to the magnetosphere of $\sim$1 h. Consequently, the magnetic activity indices AL and AU showed an increased disturbance due to a substorm just after 10 UT. The planetary K index at this time was 4. Figure 1 shows the magnetometer data from the Geophysical Institute Magnetometer Array (GIMA) site at Poker Flat. The top panel displays the H component of the magnetic field for the time period 09:48 UT–10:48 UT and the bottom panel shows the same data for the full day. A sharp negative gradient is detected at 10:03 UT, marking the onset of the substorm (red, dashed line in top panel). The total decrease of the H component is about 500 nT, and is followed by a geomagnetically disturbed period lasting for several hours. The time period of the optical data is indicated with a green block in both plots.

2.2. High-Speed Imager

[6] A high-speed imager was deployed at the T. Neil Davis Science Operations Center at Poker Flat Research Range in Alaska during a few weeks of an observational campaign. The system consists of the Andor Neo sCMOS (scientific Complementary Metal Oxide Semiconductor) detector, equipped with a 25 mm lens and a BG3 glass filter to suppress the long-lived oxygen emissions at 557.7 nm and 630.0 nm. Figure 2 illustrates the transmission of the filter (black plot) and the quantum efficiency of the sCMOS detector (red plot) overlaid on a modeled auroral spectrum showing the main molecular nitrogen emission bands and atomic oxygen peaks at arbitrary intensity (blue plot). The detector chip is an array of 2560 × 2160 pixels, with a pixel size of 6.5 μm, giving a total field of view (FOV) of 33° × 29°. The spatial resolution at auroral altitudes (100 km) is 25 m, and the camera is run in burst mode at very high temporal resolution. The data discussed here was captured at 50 frames per second, during an interval of 12 s (10:06:09.60 UT–10:06:21.42 UT). The short-time span of the burst is due to the limited camera memory of 4 GB. This is to our knowledge the highest reported cadence of auroral imaging of a substorm breakup at megapixel resolution.

3. Results

[7] The optical data provide detailed images of the evolution of the auroral display 3 min after onset of the substorm. Figure 3 is a snapshot taken at 10:06:14.2 UT. The 12 s of optical data show a highly dynamic display of auroral fine scale structures. The narrowest bright structures measured in magnetic zenith have widths perpendicular to the background magnetic field of as small as 200 m. Simultaneous with these, extended rays can be seen off zenith, in which flaming auroras are present, with emissions
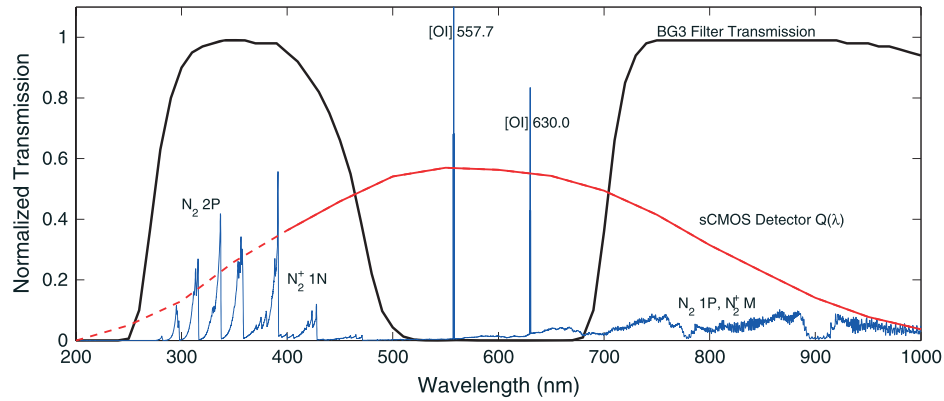
Figure 2. Transmission function of the BG3 filter (black, solid plot) and quantum efficiency of the detector (red plot) as a function of wavelength, illustrating how the filter blocks auroral emissions from the long-lived green and red oxygen lines at 557.7 nm and 630.0 nm. The quantum efficiency is only available down to 400 nm by the manufacturer of the detector and has been extrapolated for shorter wavelengths.

converging toward the center due to perceived motion of the emissions upward along the magnetic field. A video of a sequence of the data can be downloaded from the supporting information.

3.1. Analysis of Flaming Aurora

[8] Apparent streaming motion of the aurora along the rays, from the edges of the imager field of view toward the center, is detected throughout the 12 s of optical data. Four different flaming rays were selected for detailed analysis. The events were selected since they were fairly well isolated from other rays, thus reducing the background noise and any influence from superimposing structures. The chosen events are representative examples of all the flames present in the time period. Events A and B occurred between 10:06:11.9 UT and 10:06:12.4 UT, and the locations of the rays are marked in the left panel of Figure 4 with a solid and dotted box, respectively. Event A took place furthest from magnetic zenith, marked with a red circle. The intensity is integrated in azimuthal direction over the ray, and the emission intensity of the ray as a function of time and radial distance from magnetic zenith is investigated. By assuming that the altitude of the emission peak at the beginning of the flaming is 120 km (see section 5.1 for a discussion), the radial distance can be translated to apparent altitude, if it is also assumed that the ray has no horizontal motion. There is an ambiguity between the horizontal and vertical motion in the plane that intersects the arc and the camera location. To fully resolve the motion of the auroral emission, stereographic or tomographic observations made by two or more optical measurements some distant apart are needed. However, the relative magnitudes of horizontal versus vertical motion can be assessed by comparing oblique and zenith observations, under the assumption that all auroras in the field are governed by the same basic physics. The horizontal translation is found to be negligible compared to the apparent flaming motion.

[9] Figure 5, top left panel, is a time-brightness history (keogram) of a cut along the flaming ray for event A, where the emission is plotted as a function of time and converted altitude, assuming a peak height of the emission at the start of the flaming of 120 km. For each instant of time and

position along the ray, the intensity in 60 pixels across the ray was integrated and corrected for the difference in cross section of the ray (at higher altitudes the optical path through the ray is longer). The brightest structure is seen to move to higher altitudes over a time period of less than half a second. The bottom left panel is the altitude profiles of the same time interval, where the maximum brightness for each profile is marked with a red star. The peak of the brightness progressed upward along the magnetic field line, from an assumed lower altitude of 120 km to 140 km. A linear fit to the maximum of each profile gives an upward velocity of the emissions of 80 ± 12 km/s. Event B occurs at the same time, but closer to magnetic zenith, as shown in Figure 4. Figure 5 shows the intensity keogram (top right panel) and the altitude line plots (bottom right panel) for each time step. The fitted line to the maximum emission brightness gives an
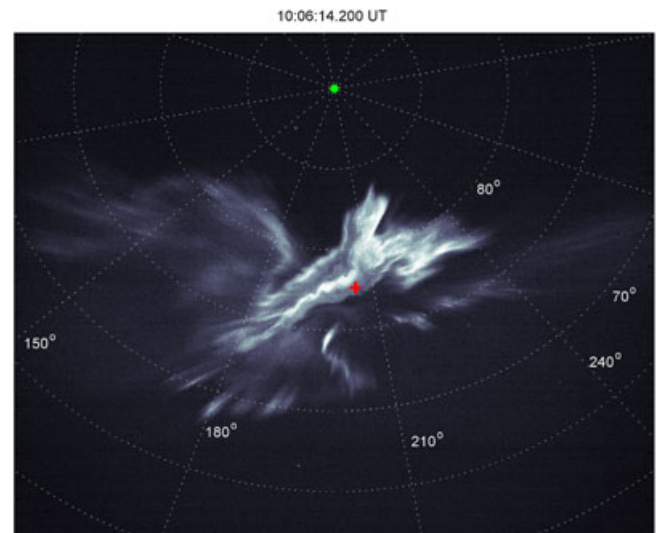

Figure 3. Captured image from the high-speed imager at 10:06:14.2 UT. Local zenith is marked with a green dot in the top of the image and elevation and azimuth angles are indicated with white-dotted lines. The red cross marks the location of magnetic zenith over Poker Flat at elevation angle 77.5° and azimuth 205.7° East of North.
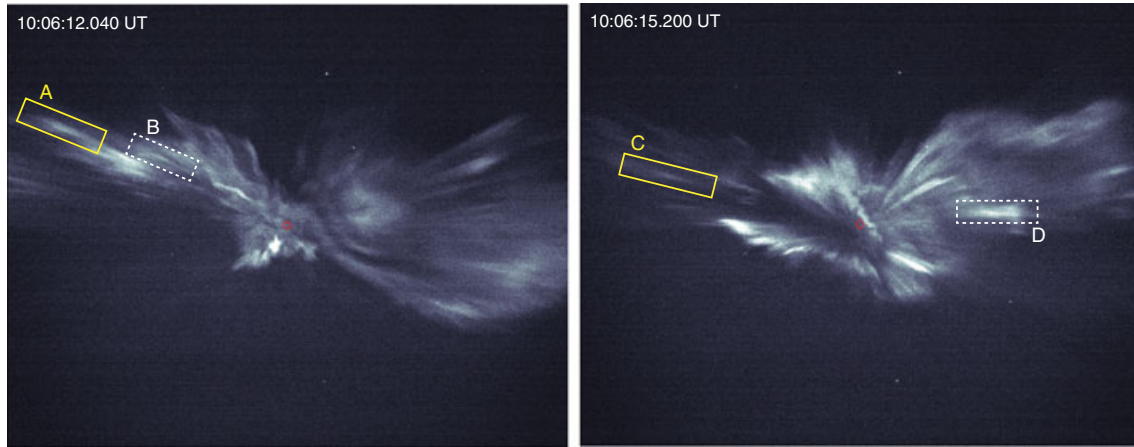
Figure 4. CMOS images with the four flaming rays marked. Most of the rays experienced flaming motion at the time of observations and these events were chosen for detailed study.

upward velocity of 93 ± 19 km/s for this auroral ray. The same analysis was made for two flaming auroral rays a few seconds later. Figure 6 shows the keograms and altitude profiles for events C and D. The linear fit to the maximum value of each profile gives upward velocities of 178 ± 31 km/s for event C and 91 ± 23 km/s for event D. Event C is shifting a larger distance, from the assumed 120 km lower altitude to 180 km, and the derived upward velocity is twice that of the other events. A reason for this could be that there is a superimposed horizontal motion, i.e., the whole ray structure could be moving in toward the center of the imager FOV, at the same time as the emission is moving upward. The widths (full-width-at-half-maximum) perpendicular to the

geomagnetic field were estimated from the images and were found to be 800 m, 840 m, 550 m, and 1140 m for events A, B, C, and D, respectively. It is noteworthy that the smallest ray is also the fastest.

3.2. Quasiperiodic Pulsations

[10] Auroral field-aligned motion is seen throughout the data sequence and most easily detected at some distance from magnetic zenith, where the view angle is more oblique. The upward motion of emission height indicates a rapid reduction in penetration depth of the causative electron beam and hence a rapid reduction in its average energy. It is thus the optical manifestation of field-aligned bursts (FABs)
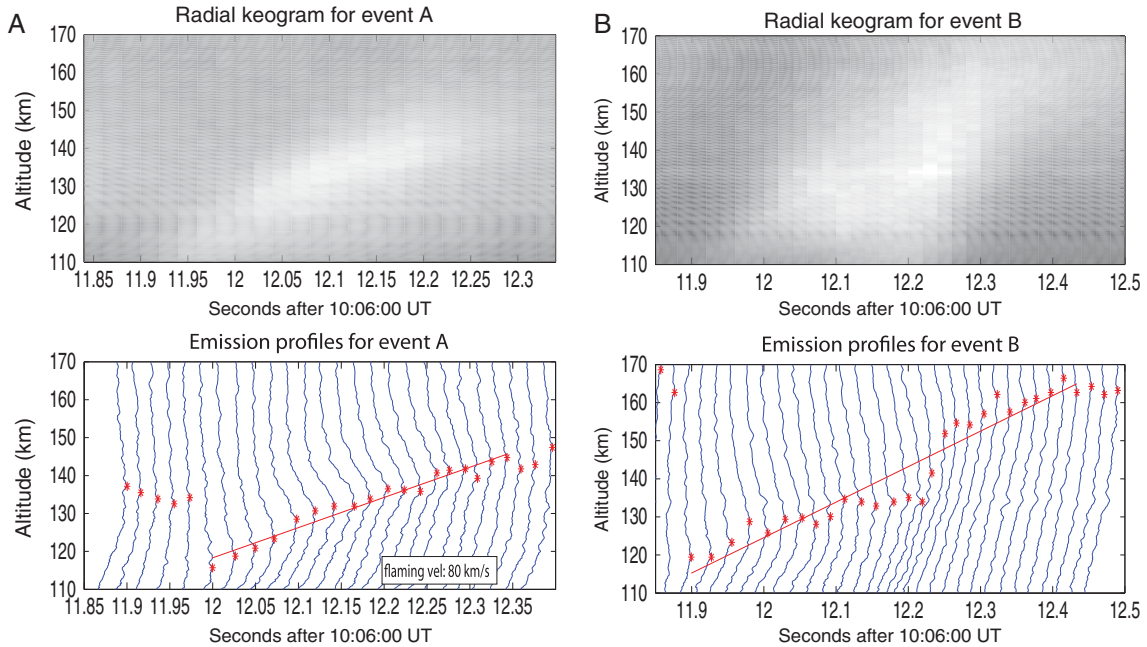

Figure 5. (top panels) Radial keograms for events A and B. The radial distance from the center of the image is translated to altitude, assuming the emission peak is at 120 km at the start of the flaming. (bottom panels) The brightness as line plots for each time, as a function of altitude is shown. The maximum brightness of each profile is marked with a red star, and a linear fit gives flaming velocities of 80 ± 12 km/s for event A and 93 ± 19 km/s for event B.
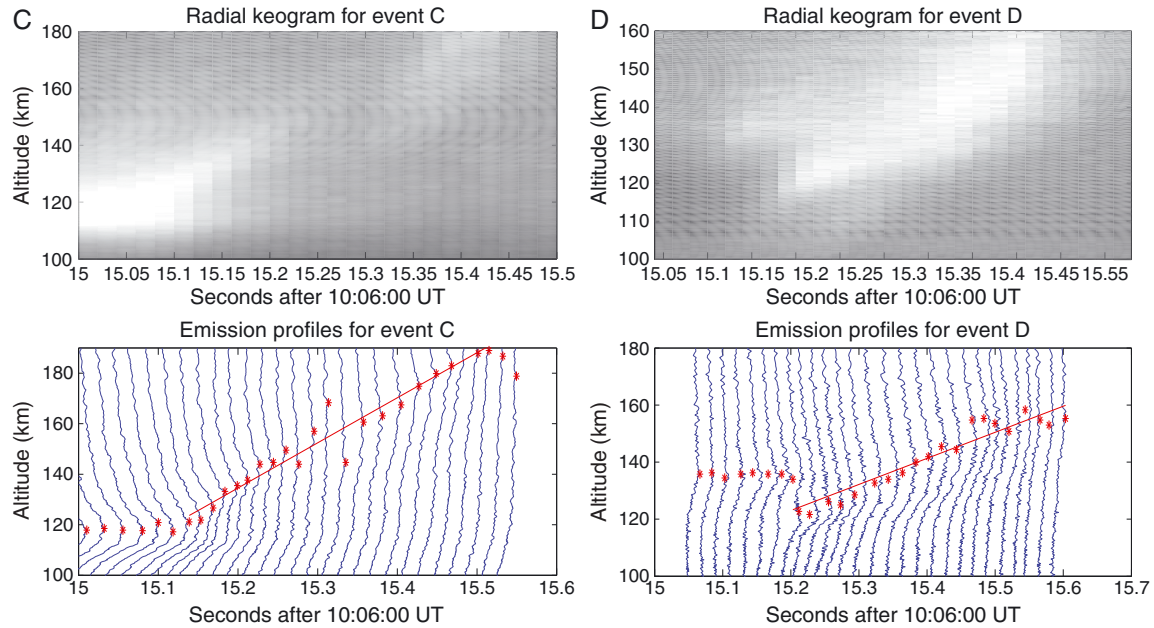
Figure 6. Same format as for Figure 5, but for events C (left panels) and D (right panels). The linear fits give flaming velocities of 178 ± 31 km/s and 91 ± 23 km/s, respectively.

commonly observed by space-borne sensors over active auroral displays [e.g., *Arnoldy et al.*, 1999; *Ivchenko et al.*, 1999]. The bursts travel up along the field lines during a time period of about 0.4 s on average for the four events. In magnetic zenith, the magnetic field lines are monitored edge on, and the signatures of auroral bursts are instead manifested as variations in the optical intensity. The top panel of Figure 7

shows the integrated intensity as measured in a region of 10×10 pixels around magnetic zenith. Quasiperiodic oscillations are seen between 10:06:13 UT and 10:06:15 UT. The corresponding power spectral density was calculated using Welch's method [*Welch*, 1967] and is shown in the bottom panel. A peak at 2.4 Hz is evident, which is consistent with a flaming repetition period of 0.4 s.
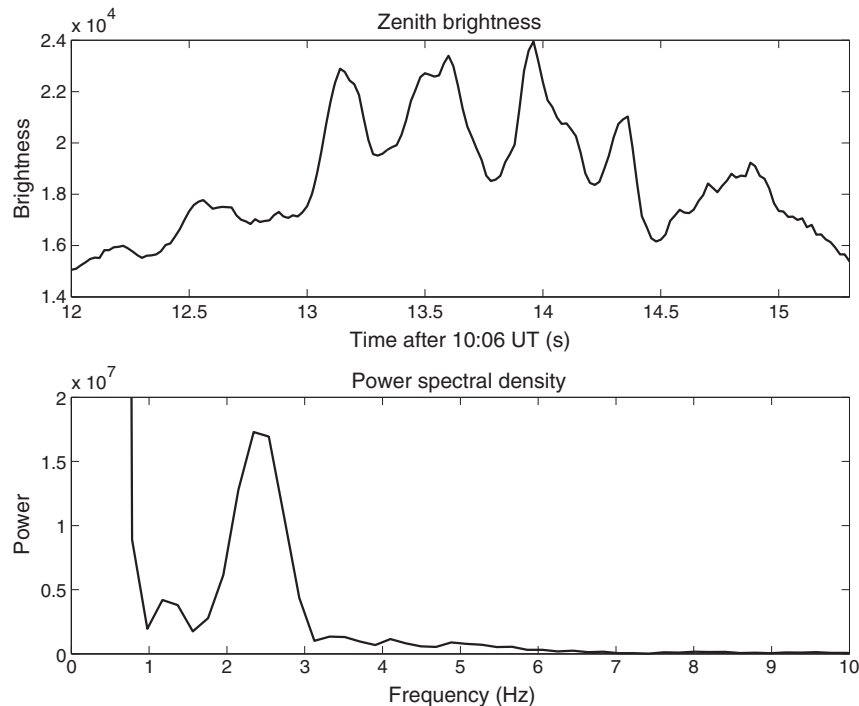

Figure 7. (top) Integrated brightness in a region of 10×10 pixels around magnetic zenith. (bottom) The power spectral density estimate shows quasiperiodic oscillations at 2.4 Hz.
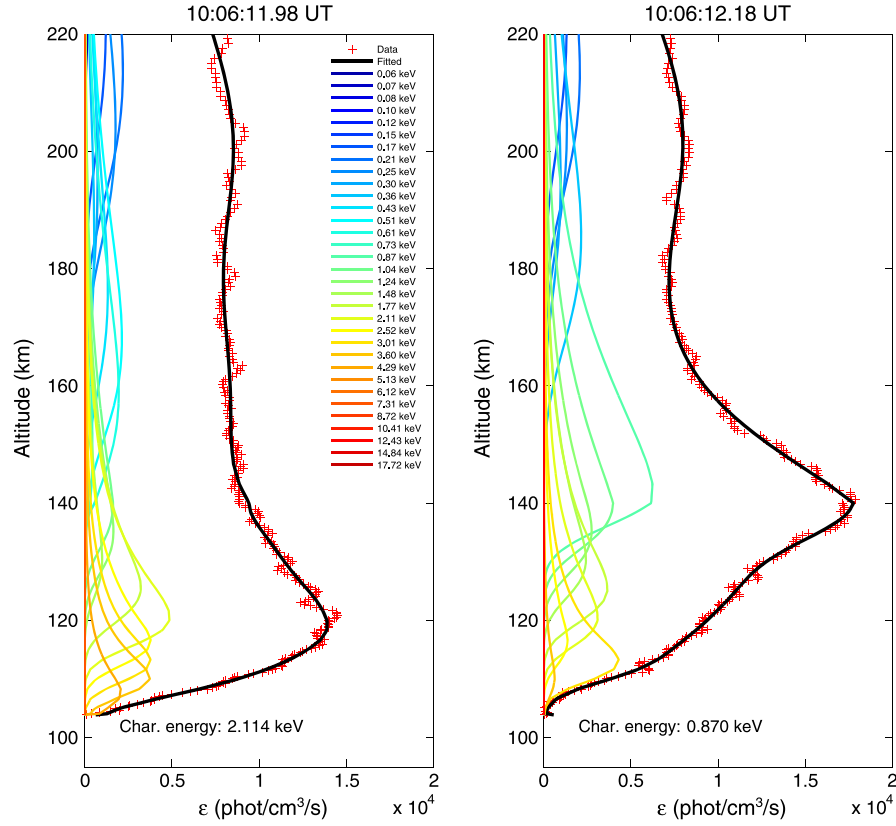
Figure 8. Measured (red) and fitted (black) volume emission rates of two instances of time for the same flame. The weighted eigenprofiles contributing to the total fitted emission rate are plotted as thinner lines in rainbow colors.

4. Estimating the Energy and Net Energy Flux of the Precipitation

[11] Investigating the nature of the electron precipitation causing the auroral features is essential to understand the exact mechanisms accelerating the electrons and the ionosphere-magnetosphere coupling. The volume emission rate as a function of altitude can be modeled with the TRANSCAR model [*Lilensten and Blelly*, 2002; *Diloy et al.*, 1996; *Blelly et al.*, 1996], in which a fluid model providing thermal electron density and temperature is coupled to a kinetic transport model, from which production and electron heating rates are obtained. The model takes in thermospheric densities and temperatures as provided by the Mass Spectrometer Incoherent Scatter (MSIS90) model [*Hedin*, 1991] with activity parameters for the date and time of the observations. By varying the input energy of the electron precipitation in discrete energy steps, eigenprofiles of volume emission rates as a function of height, energy of the precipitation, and wavelength, $M_p(z,E,\lambda)$, are produced. Further information on this eigenanalysis mode of TRANSCAR is found in *Zettergren et al.* [2007, 2008]. We use 33 log-spaced energy steps from 58 eV to 17.7 keV with differential energy flux Φ_E kept constant for each beam. The pitch-angle distribution of the electrons is field-aligned in this model run. The model produces volume emission rates for 192 different spectral features originating from the emission bands/lines of N_2^+ (1N), N_2 (1P, 2P), N_2^+ (M), O II (732–733 nm), O I (844.6 nm) and O I (777.4 nm) in the wavelength range 250–1000 nm.

[12] Since the measurements are made with a sCMOS detector fitted with a BG3 transmission filter, the modeled output profiles $M_p(z, E, \lambda)$ need to be multiplied with the quantum efficiency of the detector, $Q(\lambda_i)$, and the transmission of the filter, $T(\lambda_i)$ (see Figure 2)

$$p_{eig}(z,E) = \sum_{i=1}^{I} M_p(z,E,\lambda_i) \cdot Q(\lambda_i) \cdot T(\lambda_i) \qquad [\text{phot/cm}^3/\text{s}] \quad (1)$$

This finite set of eigenprofiles for each electron beam with energy E_n can then be linearly combined into a total volume emission rate, $p_{fit}(z)$, where each eigenprofile is weighted with a constant $k(E_n)$

$$p_{fit}(z) = \sum_{n=1}^{N} k(E_n) \; p_{eig}(z,E_n) \qquad (2)$$

A best fit between $p_{fit}(z)$ and the measured volume emission rate $p_{meas}(z)$ is determined through a linear regression analysis based on an initial estimate of the relative contribution to the weights k, with the additional constraint of positive k. The method generally results in a good fit to the measured data.

[13] The measured auroral emission profile is assumed to have its emission peak at 120 km at the start of the flaming, which then moves up along the field line over time. The auroral volume emission rate p (phot/cm³/s)
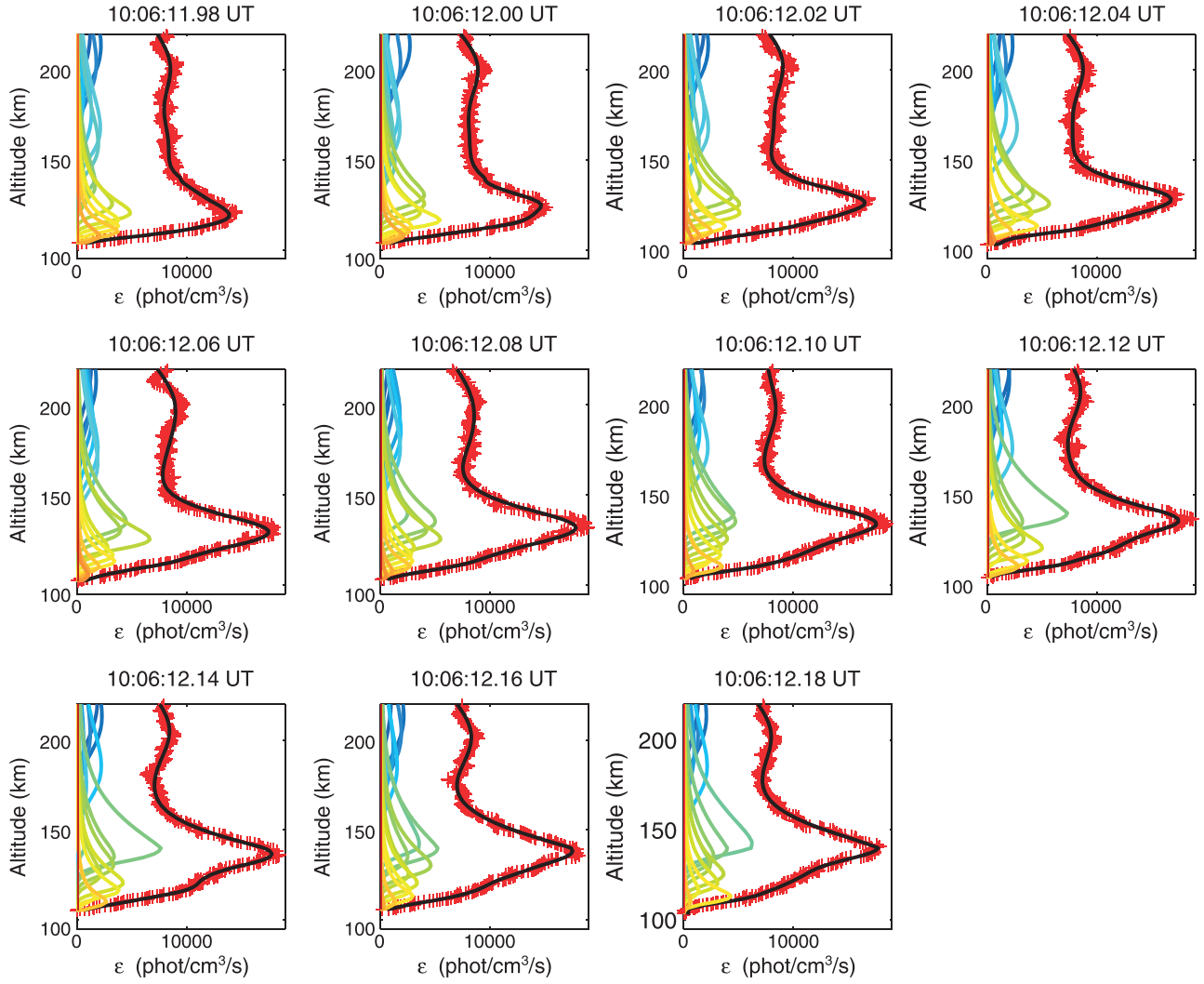
Figure 9. The temporal evolution of measured and fitted volume emission rate profiles, between 10:06:11.98 UT and 10:06:12.18 UT, in time increments of 0.02 s. The plots have the same format as Figure 8 and illustrate the good fit obtained by utilizing linear regression.

can be estimated from the measured signal S (in data numbers DN) by

$$p = \frac{SG}{\tau A_{pxl} D} \qquad (3)$$

where G is the gain of the detector, here assumed to be 2 e$^-$/DN, τ is the exposure time, A_{pxl} the detection area on the chip and D the thickness of the auroral ray that the emission is integrated over. To increase the signal, we have binned 60 × 2 pixels into one superpixel, with the 60 pixels being taken along a cut perpendicular to the auroral ray of interest. Each pixel has a physical size on the chip of 6.5 µm × 6.5 µm. The exposure time of the data is $\tau = 0.02$ s, and the thickness of the auroral rays D is estimated to be 8×10^4 cm.

[14] The volume emission rates as a function of altitude for flame A are shown in Figure 8, for two different times, separated by 0.2 s. The red ++ line is the measured data, and the thick black line is the fitted $p_{fit}(z)$, which is built up by the eigenprofiles shown as thinner lines in rainbow colors, one for each individual beam of energy. The peak of the emission is clearly shifted up in altitude over the short time interval, and the precipitation is found to be

distributed over a large range of energies. The energy of the eigenprofile with the largest weight k and thus characteristic energy of the ray (printed in each figure) is found to decrease over time.

[15] The volume emission rate profiles have been fitted in the same way with the modeled composition of the monoenergetic eigenprofiles weighted with k for 11 time steps of the duration of the flaming ray. The time evolution of the energy distribution of the weight is shown in Figure 9.

[16] The characteristic energy E_0 of the electron precipitation is a measure of the energy gained by the distribution in the acceleration process of the electrons along the magnetic field line and is defined as the energy of the suprathermal peak (bump-on-tail above an energy of 500 eV in the energy flux spectrum) of the electron energy distribution [*Semeter and Kamalabadi*, 2005]:

$$E_0 = \underset{E_j > 500}{\arg\max} \ (\Phi_E(E_j)) \qquad [\text{eV}] \qquad (4)$$

[17] The characteristic energy at the start of event A, 10:06:11.98 UT, is 2.1 keV, and at 10:06:12.18 UT it has
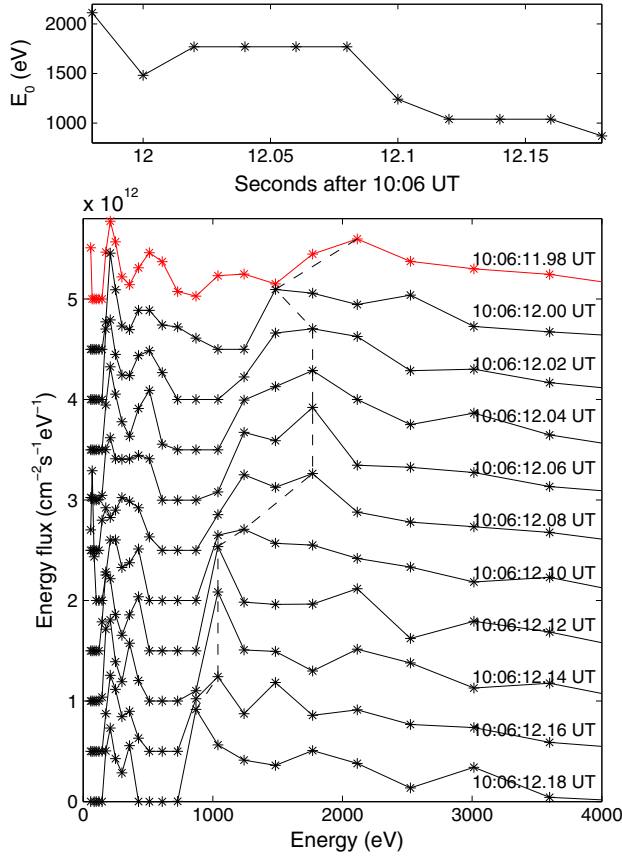
Figure 10. (top panel) Flame A experiences a decrease in characteristic energy from 2.1 keV to 0.87 keV during its 0.2 s lifetime. (bottom panel) Electron energy flux versus energy for the 11 time steps (from top to bottom) of the evolution of the flame, illustrating the steady decrease in characteristic energy with time (outlined with a dashed line). The first profile is plotted with an offset of 5×10^{12} cm^{-2}s^{-1}eV^{-1}, and each following plot has a decreased offset of 5×10^{11} cm^{-2}s^{-1}eV^{-1} to visualize them in the same plot.

decreased to 0.87 keV. Figure 10, top panel, shows this decrease of E_0 with time for this ray. The bottom panel shows the modeled electron energy flux as a function of energy for the 11 time steps, plotted with an offset with respect to each other. The top plot (in red, with an offset of 5×10^{12} cm^{-2}s^{-1}eV^{-1}) is the distribution at the start time 10:06:11.98 UT. The suprathermal peak of the distribution is evident around 2.1 keV, and the temporal evolution shows how its peak (characteristic energy) shifts to lower energies over time (also outlined with a dashed line in the figure).

[18] From the individual differential number flux ϕ_N of each eigenprofile, the net energy flux ϕ_e of the precipitation is then obtained from

$$\phi_e = \sum_{j=1}^{33} k(E_j)\, \phi_N(E_j)\, E_j\, \Delta E_j \qquad (5)$$

[19] The resulting net energy flux is on average 10.8 mW/m^2 for flame A.

5. Discussion

5.1. Height of the Emissions

[20] The apparent upward motion of the flaming aurora is the result of low energy electrons reaching the ionosphere after the faster high energy electrons, which also penetrate to lower altitudes. Some assumptions about the data were necessary to estimate the energy and flux of the precipitation causing the optical emissions analyzed here, with the most crucial assumption being the auroral emission height at the start of the flaming surge. From the monostatic optical data, it is not possible to measure this height, stereographic measurements would be needed. However, the collocated Poker Flat Incoherent Scatter Radar (PFISR) was operating at the time of the observations, providing measurements of the altitude variation of ionospheric plasma parameters such as electron density. PFISR was running a five beam configuration 480 μs long pulse experiment, resulting in a crude range resolution of the measurements of 72 km, with one beam pointed along the geomagnetic field. At the time of the flames, naturally enhanced ion acoustic lines were present in the radar echoes, which further complicated the fitting of plasma parameters for this time. Due to this, the unprocessed raw power profiles returned by the radar were investigated, which are sampled at a higher frequency (30 μs), rather than the usual integrated fitted spectra. The raw power is an estimate of the electron density, under the assumption that the ion and electron temperatures are equal. The black profile in Figure 11 shows the electron density altitude profile from the PFISR beam in magnetic zenith. The data have been averaged over 5 s, under which time several flaming rays would have been formed at lower altitudes and moved up along the magnetic field lines, smearing the electron density estimates in height.

[21] The auroral emissions are proportional to the ionization rate, which in steady state in the ionospheric E region and when assuming charge neutrality can be approximated with an effective recombination rate times the square of the electron density,

$$q(z) = \alpha_{\text{eff}}(z) n_e(z)^2 \qquad (6)$$

By averaging the volume emission rate profiles shown in Figure 9 for flame A, an estimate of the total ionization rate is obtained from the optical data. The electron density profile for this event can then be calculated from equation (6) using the effective E region recombination rate

$$\alpha_{\text{eff}}(z) = 2.5 \times 10^{-12} e^{-z/51.2} \quad [\text{m}^3/\text{s}] \qquad (7)$$

where z is in km [*Semeter and Kamalabadi*, 2005]. To be able to compare the electron density from optical measurements with the radar profile, the optical profile is convoluted with a 72 km long boxcar function to resemble the smoothing due to the pulse length of the sampled radar data.

[22] This simple model to estimate the electron density profiles from the optical emissions is only valid under the assumption of steady state ($dn_e/dt = P - L = 0$) with electron production P and losses L considered equal during a 5 s long-time period corresponding to the time integration of the radar data. Such an assumption is somewhat difficult to justify during an active auroral display, and the emission height analysis presented here should therefore be interpreted with caution. In addition, the ionization source
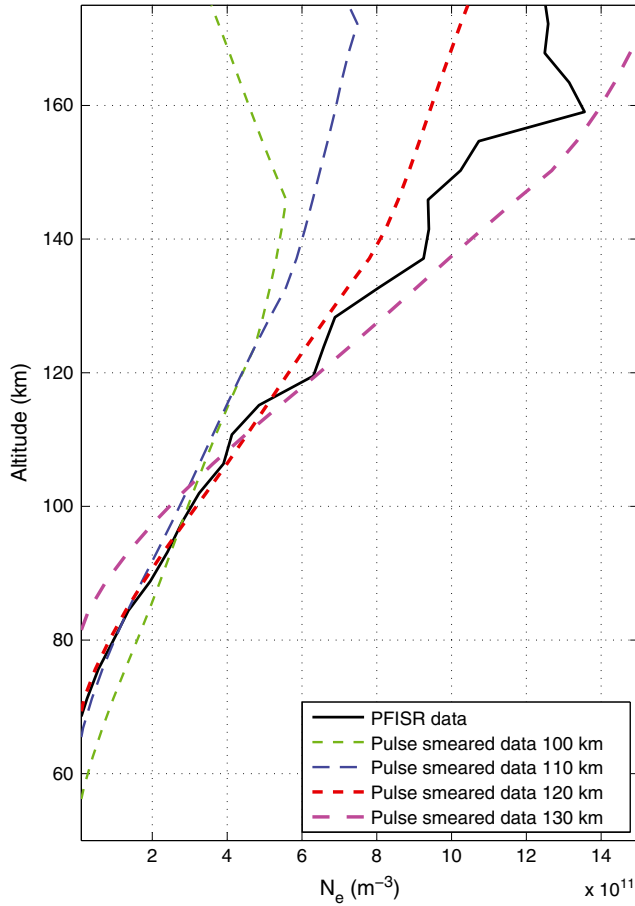
Figure 11. Electron density profiles derived from PFISR raw data (black, solid plot) and from the observed volume emission rates (dashed plots) when different emission peak altitudes at the start of the flaming ray are assumed. The best fit with the radar data at lower altitudes is found for an assumed start emission peak at 120 km (red, dashed plot).

varies rapidly compared to the recombination rate (a few seconds) at 110 km, but the variation time scale is similar to the recombination time in the 60–80 km range. The assumption of steady state, with the production rate being equal to the loss rate, is thus foremost valid at lower altitudes. The electron density profile from radar measurements is therefore expected to have a higher correlation with the profile derived from optical measurements in the D and lower E regions. The pulse-smeared electron density profiles from a number of optical measurements are plotted as dashed lines in Figure 11, for model runs where the emission peak of the flaming rays started at 100 km, 110 km, 120 km, and 130 km, respectively. Each curve has been scaled by a constant factor until a best fit with the radar profile (solid plot) at altitudes below 120 km was found. The need of a scaling factor is explained by, for example, possible discrepancies due to the different time integrations of radar and optical data, the assumed recombination rate, and foremost that the radar and optical measurements are from two different pointing directions, the radar beam is pointing in magnetic zenith whereas the optical data originate from a different flaming ray observed at an oblique angle. However, the scaling factors do not change the overall shape of the profiles.

The best fit is found for the optical profile where the start emission height of 120 km was used (red profile), which justifies the choice of this emission altitude as start altitude in the analysis of the flaming rays (section 3.1), within these mentioned assumptions.

[23] Apart from the assumption of emission heights of the aurora, other possible sources of errors in the analysis originate, for example, from only including the brightest emission bands and peaks in the TRANSCAR model, thus neglecting any contributions from fainter emissions such as from molecular oxygen or OH bands. Errors may also originate from using the MSIS atmosphere model for the neutral atmospheric composition during a geomagnetically disturbed period. Atmospheric absorption has not been taken into account, which is particularly strong at shorter wavelengths. In addition, the quantum efficiency of the sCMOS detector is not available below 400 nm and has been extrapolated in this wavelength region. Errors originating from the conversion of data numbers to photon/cm^3/s are of less importance for the energy analysis, since it is foremost the altitude dependence and shape of the volume emission rate that gives the estimated energy of the precipitation, whereas the magnitude of the volume emission rate will affect the estimate of the net energy flux. Despite all these sources of uncertainty, the energy analysis shows a general consistency and it is possible to see a trend in the evolution of the flaming rays, which indicates that the method is valid to the first order for high-resolution energy analysis of rays observed from the ground.

5.2. Acceleration Mechanisms and Source Region

[24] If electrons of different energy were released from one source point along the geomagnetic field, confined in the temporal and spatial dimension, the resulting ionospheric signature would be the kind of dispersion and flaming aurora that we observe. The common source height H can be estimated from the time difference δt between the initial electrons at 10:06:11.98 UT with velocity $v_1 = \sqrt{2E_1/m_e}$ and the less energetic electrons at 10:06:12.18 UT which traveled a distance $H - \Delta H$ with velocity v_2

$$H = \frac{\delta t\, v_2 + \Delta H}{1 - \frac{v_2}{v_1}} \tag{8}$$

The stop height difference ΔH for event A is 20 km, and the source region is thus estimated to be approximately at 1.55 R$_E$ (9900 km) altitude.

[25] However, electron energies spanning a broad range of energies from a few tens of eV up to several keV are a typical signature of electron acceleration by Alfvén waves, as seen both by in situ observations from rockets and satellites as well as produced by models [e.g., *Arnoldy et al.*, 1999; *Ivchenko et al.*, 1999, *Chasten et al.*, 2000, 2002; *Kletzing and Hu*, 2001]. Dispersive Alfvén waves with short perpendicular scale lengths can carry an electric field parallel to the magnetic field, which resonantly accelerates electrons over a large distance along the magnetic field lines [*Hasegawa*, 1976]. Alfvén wave models have also been able to show that the wave-particle interaction can result in dispersed electron signatures [*Kletzing and Hu*, 2001; *Andersson et al.*, 2002]. The acceleration of electrons cannot then be considered as taking place in one point in time and space, instead the acceleration is time-dependent and occurs over a large

range along the magnetic field lines, where the Poynting flux of kinetic Alfvén waves is dissipated to the electrons.

[26] The acceleration process by Alfvén waves has been investigated with pure fluid models, particle-in-cell simulations, and with models including the kinetic effects of the hot electrons [e.g., *Hui and Seyler*, 1992; *Thompson and Lysak*, 1996; *Rankin et al.*, 1999]. The observed dispersions in this study show time delays of the same order of magnitude as in the simulations. *Andersson et al.* [2002] used a simplistic model of the velocities of electrons accelerated by an Alfvén wave where the wave was considered a potential drop moving with the Alfvén speed. The acceleration process was not analyzed, instead the acceleration was assumed to result in electrons moving with twice the Alfvén speed which has the maximum at an altitude of just below 1 R_E. A similar acceleration was also found in the particle-in-cell simulations by *Seyler and Liu* [2007]. The energy dispersion observed here is somewhat more rapid than the example studied by *Andersson et al.* [2002], with a faster decrease in energy over time. Such fast dispersions indicate a source closer to the ionosphere, which could be difficult to resolve in satellite data. Optical measurements provide new possibilities to investigate also the fastest dispersions.

[27] It is possible that in addition to the wave-particle interaction, the electrons are also energized by a quasi-static potential drop. *Arnoldy et al.* [1999] and *Semeter et al.* [2001] analyzed data from the PHAZE II rocket to investigate similar energy-dispersed FABs that were coincident with pitch-angle dispersed electrons accelerated by an inverted-V potential. The FABs had energies in the same range as observed in this study, consisting of bursts of cold ionospheric electrons. Although it is somewhat difficult to discern the dispersion at a few keV energies from the PHAZE II data due to the cruder resolution of the rocket measurements, the time lag of 0.2 s found here seem to be somewhat longer but of the same order as that detected by the electron detectors in situ (approximately 0.1 s).

[28] Wave-particle acceleration mechanisms have also been suggested to take place further out in the magnetosphere in the plasma sheet boundary layer (PSBL), in addition to the particle energization at and below 1 R_E altitude. Strong Alfvenic turbulence is commonly observed in the PSBL at 4–6 R_E geocentric distance with the Polar spacecraft during the expansion phase of substorms [*Wygant et al.*, 2002; *Keiling et al.*, 2005]. *Lessard et al.* [2011] found a relationship between Pi1B pulsations originating from beyond geosynchronous orbit and wave-driven aurora during the onset of a substorm, suggesting that the pulsations propagating from the magnetotail are powering the aurora. Pi1B pulsations are bursty waves with frequencies from 25 mHz to 1 Hz; sometimes higher frequencies are seen too. Similarly, *Arnoldy et al.* [1987] earlier established that Pi1B pulsations can be highly correlated with the changes in auroral luminosity during a substorm. The auroral emissions in this study contain oscillations with a frequency of 2.4 Hz (Figure 7), which is consistent with Pi1B pulsations, albeit somewhat on the high end. The Pi1B signatures are further supported by the University of New Hampshire induction coil magnetometer at Poker Flat, showing clear signatures of Pi1B pulsations at the time of the optical observations. This indicates that even though the acceleration takes place by wave-particle interactions in the region of up to a few R_E

above the ionosphere, the Alfvén waves could be powered by pulsations originating from the magnetotail, most likely caused by the dipolarization of the geomagnetic field during the substorm onset.

[29] The 2.4 Hz oscillations are slower than the oscillations of the FABs measured by the PHAZE II electron analyzer [*Arnoldy et al.*, 1999], which showed a frequency of 10 Hz. In their study, it was argued that the acceleration was due to combined wave activity and a quasi-static potential drop, and that the oscillations resulted from the potential switching on and off. Two minutes later, the data contained oscillations with a lower frequency of 3–6 Hz occurring outside the inverted-V [*Semeter et al.*, 2001], and the time dispersion of this sequence indicates a source height between 3000 and 6000 km. Electron bursts with a slower oscillation frequency have also been noted by *Lynch et al.* [1999], who studied dispersion signatures at the poleward edge of an inverted-V arc from the Auroral Turbulence II rocket flight. The bursts had a frequency of 0.65 Hz, and the source height was derived to 1.5–3.1 R_E. Again, superimposed signatures of both Alfvén wave acceleration and acceleration by a quasistatic potential drop were detected. During optical ground-based observations of an auroral post-breakup event, *Semeter et al.* [2008] detected 6 Hz oscillations at the edge of the narrow-field optical detector. The conditions were similar to the observations in this study, and flaming aurora was detected in the data. The emission profiles analyzed in this study show no clear indication of acceleration by a potential drop. The frequency falls within the definition of flickering aurora (2–20 Hz), which is believed to be due to a modulation of O^+ cyclotron waves above the ionosphere [*Temerin et al.*, 1986]. The 2.4 Hz frequency corresponds roughly to the O^+ cyclotron frequency at 8700 km altitude.

6. Conclusions

[30] In this paper, we show a substorm expansion phase event of auroral rays containing surges of luminosity traveling upward along the magnetic field lines, consistent with electron energy dispersions and energies covering a large range from a few tens of eV up to several keV. This phenomenon has been coined flaming aurora when observed from the ground, and FABs when measured in situ. This study presents to our knowledge the first systematic and quantitative interpretation of such optical auroral features in the context of FABs. We have shown optical evidence that these FABs are coincident with discrete breakup arcs and dispersive Alfvén waves, and that with high-resolution optical measurements from the ground, it is possible to estimate the energy dispersion of bursty electron precipitation at very high time and energy resolution. Unlike rocket or satellite measurements where an auroral arc is traversed in time scales of up to a second, ground-based optical data can fully resolve the spatio-temporal signatures and investigate the reoccurrence of emissions in the same region. The optical diagnostic presented here makes use of model-based inversion of auroral signatures to derive the spatiotemporal variations of the differential energy flux spectrum. However, for the present analysis, an assumption of the emission height must be made, which will affect the derived parameters of the emission bursts. Stereographic measurements from the ground would be an important asset for future

measurements to determine the emission height. With this assumption, we find that during a time period of 0.2 s the characteristic energy of one flaming ray decreases rapidly from 2.1 keV to 0.87 keV. The dispersion signatures indicate a source region of about 10^4 km altitude, but it is likely that the acceleration in this region takes place over a large distance, through Alfvén wave interactions, resulting in energies ranging from a few tens of eVs to a few keV. Pi1B pulsations seen simultaneously indicate that the waves could have been powered from far out in the magnetotail during this substorm expansion phase. Using high-resolution optical data is thus an efficient method to get a detailed view of the spatio-temporal variations of low energy precipitation in aurora.

References

Andersson, L., N. Ivchenko, J. Clemmons, A. A. Namgaladze, B. Gustavsson, J.-E. Wahlund, L. Eliasson, and R. Y. Yurik (2002), Electron signatures and Alfvén waves, *J. Geophys. Res.*, *107*(A9), 1244, doi:10.1029/2001JA900096.

Arnoldy, R. L., R. Rajashekar, L. J. Cahill, M. J. Engebretson, and T. J. Rosenberg (1987), Simultaneous measurement of aurora-related, irregular magnetic pulsations at northern and southern high latitudes, *J. Geophys. Res.*, *92*, 12,221–12,232, doi:10.1029/JA092iA11p12221.

Arnoldy, R. L., K. A. Lynch, J. B. Austin, and P. M. Kintner (1999), Energy and pitch angle-dispersed auroral electrons suggesting a time-variable, inverted-V potential structure, *J. Geophys. Res.*, *104*, 22,613–22,622, doi:10.1029/1999JA900219.

Blelly, P.-L., J. Lilensten, A. Robineau, J. Fontanari, and D. Alcaydé (1996), Calibration of a numerical ionospheric model with EISCAT observations, *Ann. Geophys.*, *14*, 1375–1390, doi:10.1007/s00585-996-1375-x.

Chaston, C. C., C. W. Carlson, R. E. Ergun, and J. P. McFadden (2000), Alfvén waves, density cavities and electron acceleration observed from the FAST spacecraft, *Phys. Scr.*, *84*, 64–68.

Chaston, C. C., J. W. Bonnell, L. M. Peticolas, C. W. Carlson, and J. P. McFadden (2002), Driven Alfven waves and electron acceleration: A FAST case study, *Geophys. Res. Lett.*, *29*, 1535–1538, doi:10.1029/2001GL013842.

Cresswell, G. R. (1969), Flaming auroras, *J. Atmos. Sol. Terr. Phys.*, *31*, 179–183.

Diloy, P.-Y., A. Robineau, J. Lilensten, P.-L. Blelly, and J. Fontanari (1996), A numerical model of the ionosphere, including the E-region above EISCAT, *Ann. Geophys.*, *14*, 191–200, doi:10.1007/s00585-996-0191-7.

Goertz, C. K. (1981), Discrete breakup arcs and kinetic Alfvén waves, Physics of Auroral Arc Formation, *Geophys. Monogr. Ser.*, *25*, 451–455.

Hallinan, T. J., and T. N. Davis (1970), Small-scale auroral arc distortions, *Planet. Space Sci.*, *18*, 1735–1735, doi:10.1016/0032-0633(70)90007-3.

Hasegawa, A. (1976), Particle acceleration by MHD surface wave and formation of aurora, *J. Geophys. Res.*, *81*, 5083–5090, doi:10.1029/JA081i028p05083.

Hedin, A. E. (1991), Extension of the MSIS thermosphere model into the middle and lower atmosphere, *J. Geophys. Res.*, *96*, 1159–1172.

Hui, C.-H., and C. E. Seyler (1992), Electron acceleration by Alfven waves in the magnetosphere, *J. Geophys. Res.*, *97*, 3953–3963, doi:10.1029/91JA03101.

Ivchenko, N., G. Marklund, K. Lynch, D. Pietrowski, R. Torbert, F. Primdahl, and A. Ranta (1999), Quasiperiodic oscillations observed at the edge of an auroral arc by Auroral Turbulence 2, *Geophys. Res. Lett.*, *26*, 3365–3368, doi:10.1029/1999GL003588.

Keiling, A., G. K. Parks, J. R. Wygant, J. Dombeck, F. S. Mozer, C. T. Russell, A. V. Streltsov, and W. Lotko (2005), Some properties of Alfvén waves: Observations in the tail lobes and the plasma sheet boundary layer, *J. Geophys. Res.*, *110*, A10S11, doi:10.1029/2004JA010907.

Kletzing, C. A., and S. Hu (2001), Alfvén wave generated electron time dispersion, *Geophys. Res. Lett.*, *28*, 693–696, doi:10.1029/2000GL012179.

Lessard, M. R., E. J. Lund, H. M. Kim, M. J. Engebretson, and K. Hayashi (2011), Pi1B pulsations as a possible driver of Alfvénic aurora at substorm onset, *J. Geophys. Res.*, *116*, A06203, doi:10.1029/2010JA015776.

Lilensten, J., and P. L. Blelly (2002), The TEC and F2 parameters as tracers of the ionosphere and thermosphere, *J. Atmos. Sol. Terr. Phys.*, *64*, 775–793, doi:10.1016/S1364-6826(02)00079-2.

Lynch, K. A., D. Pietrowski, R. B. Torbert, N. Ivchenko, G. Marklund, and F. Primdahl (1999), Multiple-point electron measurements in a nightside auroral arc: Auroral turbulence II particle observations, *Geophys. Res. Lett.*, *26*, 3361–3364, doi:10.1029/1999GL900599.

Omholt, A. (1971), *The Optical Aurora*, 198 pp., Springer, Berlin.

Rankin, R., J. C. Samson, and V. T. Tikhonchuk (1999), Parallel electric fields in dispersive shear Alfvén waves in the dipolar magnetosphere, *Geophys. Res. Lett.*, *26*, 3601–3604, doi:10.1029/1999GL010715.

Rees, M. H. (1964), Ionization in the Earth's atmosphere by aurorally associated Bremsstrahlung X-rays, *Planet. Space Sci.*, *12*, 1093–1108, doi:10.1016/0032-0633(64)90084-4.

Semeter, J., and F. Kamalabadi (2005), Determination of primary electron spectra from incoherent scatter radar measurements of the auroral E region, *Radio Sci.*, *40*, RS2006, doi:10.1029/2004RS003042.

Semeter, J., J. Vogt, and G. Haerendel (2001), Persistent quasiperiodic precipitation of suprathermal ambient electrons in decaying auroral arcs, *J. Geophys. Res.*, *106*, 12,863–12,873, doi:10.1029/2000JA000136.

Semeter, J., M. Zettergren, M. Diaz, and S. Mende (2008), Wave dispersion and the discrete aurora: New constraints derived from high-speed imagery, *J. Geophys. Res.*, *113*, A12208, doi:10.1029/2008JA013122.

Seyler, C. E., and K. Liu (2007), Particle energization by oblique inertial Alfvén waves in the auroral region, *J. Geophys. Res.*, *112*, A09302, doi:10.1029/2007JA012412.

Temerin, M., J. McFadden, M. Boehm, C. W. Carlson, and W. Lotko (1986), Production of flickering aurora and field-aligned electron flux by electromagnetic ion cyclotron waves, *J. Geophys. Res.*, *91*, 5769–5792, doi:10.1029/JA091iA05p05769.

Thompson, B. J., and R. L. Lysak (1996), Electron acceleration by inertial Alfvén waves, *J. Geophys. Res.*, *101*, 5359–5369, doi:10.1029/95JA03622.

Trondsen, T. S., and L. L. Cogger (2001), Fine-scale optical observations of Aurora, *Phys. Chem. Earth (C)*, *26*, 179–188, doi:10.1016/S1464-1917(00)00105-7.

Welch, P. D. (1967), The use of fast Fourier transform for the estimation of power spectra: A method based on time averaging over short, modified periodograms, *IEEE Trans. Audio Electroacoust.*, *15*, 70–73, doi:10.1109/TAU.1967.1161901.

Wygant, J. R., et al. (2002), Evidence for kinetic Alfvén waves and parallel electron energization at 4–6 R_E altitudes in the plasma sheet boundary layer, *J. Geophys. Res.*, *107*, 1201, doi:10.1029/2001JA900113.

Zettergren, M., J. Semeter, P.-L. Blelly, and M. Diaz (2007), Optical estimation of auroral ion upflow: Theory, *J. Geophys. Res.*, *112*, A12310, doi:10.1029/2007JA012691.

Zettergren, M., J. Semeter, P.-L. Blelly, G. Sivjee, I. Azeem, S. Mende, H. Gleisner, M. Diaz, and O. Witasse (2008), Optical estimation of auroral ion upflow: 2. A case study, *J. Geophys. Res.*, *113*, A07308, doi:10.1029/2008JA013135.